Direct Ink Writing of $Li_{1.3}Al_{0.3}Ti_{1.7}(PO_4)_3$-Based Solid-State Electrolytes with Customized Shapes and Remarkable Electrochemical Behaviors

Zixian Liu, Xiaocong Tian,* Min Liu, Shanshan Duan, Yazhou Ren, Hui Ma, Kang Tang, Jianpeng Shi, Shuen Hou, Hongyun Jin,* and Guozhong Cao

All-solid-state lithium batteries have received extensive attention due to their high safety and promising energy density and are considered as the next-generation electrochemical energy storage system. However, exploring solid-state electrolytes in customized geometries without sacrificing the ionic transport is significant yet challenging. Herein, various 3D printable $Li_{1.3}Al_{0.3}Ti_{1.7}(PO_4)_3$ (LATP)-based inks are developed to construct ceramic and hybrid solid-state electrolytes with arbitrary shapes as well as high conductivities. The obtained inks show suitable rheological behaviors and can be successfully extruded into solid-state electrolytes using the direct ink writing (DIW) method. As-printed freestanding LATP ceramic solid-state electrolytes deliver high ionic conductivity up to 4.24×10^{-4} S cm^{-1} and different shapes such as "L", "T," and "+" can be easily realized without sacrificing high ionic transport properties. Moreover, using this printing method, LATP-based hybrid solid-state electrolytes can be directly printed on $LiFePO_4$ cathodes for solid-state lithium batteries, where a high discharge capacity of 150 mAh g^{-1} at 0.5 C is obtained. The DIW strategy for solid-state electrolytes demonstrates a new way toward advanced solid-state energy storage with the high ionic transport and customized manufacturing ability.

Portable devices are becoming ubiquitous and there is an ever-increasing demand for electric vehicles as well. Lithium-ion batteries (LIBs) have received enormous attention and become the most widely used power supplying sources for portable devices

and electric vehicles.[1–6] High-safety, high-capacity, low-cost, and high-life-span are always desired for LIBs.[7–11] At present, most commercial LIBs contain liquid electrolytes, which pose fire and explosion hazards to people due to their low boiling point and flash point.[12] However, solid-state electrolytes (SSEs) are able to reduce or eliminate these risks.[3,13]

SSEs can be mainly divided into solid polymer electrolytes, oxide-based SSEs, and sulfide-based SSEs.[14–16] Na superionic conductor (NASICON)-type $Li_{1.3}Al_{0.3}Ti_{1.7}(PO_4)_3$ (LATP) is a typical oxide-based SSE with high conductivity and electrochemical stability which is recognized as one of the most promising LIB electrolytes.[17–21] It is less sensitive to moisture and O_2, therefore allowing the direct preparation in open air with low-cost raw materials. Moreover, it is electrochemically stable to most cathode materials. In order to build LATP-based SSEs, various manufacturing methods have been developed to date. For the pure LATP ceramic solid-state electrolytes (CSSEs), one of the most used manufacturing methods is the tableting method, which employs a mold to press-form inorganic powder and is also termed as the subtractive manufacturing. However, for the tableting method, one molded electrolyte requires a certain mold, thus hindering the manufacturing efficiency. For LATP-based hybrid solid-state electrolytes (HSSEs), the solution-casting method was used mostly, which also needs a specific mold to get a designed film. With the rapid development of portable devices, shapes of batteries are critical for the device space saving and no longer limited to traditional cuboids or cylinders. Thus, new electrolyte manufacturing method is urgently needed to produce SSEs with designed shapes as well as high conductivities.

As an emerging additive manufacturing technology, three-dimensional (3D) printing has become a versatile tool to construct customized 3D architectures for different application fields.[22–28] This technology is conducted based on a layer-by-layer stacking principle with computer aided design (CAD). In the field of electrochemistry, 3D printing has also been applied to manufacture high-performance energy storage components with an especial focus on electrodes.[29] To date, several pioneering works based on 3D printing techniques such as direct

Z. Liu, Prof. X. Tian, S. Duan, Y. Ren, H. Ma, K. Tang,
Prof. S. Hou, Prof. H. Jin
Faculty of Materials Science and Chemistry
China University of Geosciences
Wuhan 430074, P. R. China
E-mail: tianxc@cug.edu.cn; jinhongyun@cug.edu.cn
Prof. X. Tian
Zhejiang Institute
China University of Geosciences
Hangzhou 311305, P. R. China
Dr. M. Liu, Dr. J. Shi
Department of Technology Centre of Dongfeng Motor Group Co. LTD
Wuhan 430058, P. R. China
Prof. G. Cao
Department of Materials Science & Engineering
University of Washington
Seattle, WA 98195, USA

**ADVANCED
SCIENCE NEWS**

www.advancedsciencenews.com

NANO · MICRO

small

www.small-journal.com

Figure 1. Schematic of DIW printing procedure of LATP CSSEs.

ink writing (DIW) and stereolithographic printing have turned out to be a great success for the electrode fabrication.[30–33] DIW has been acknowledged as one of most promising printing candidates due to its direct writing capability of materials with tuned chemistry. Sun et al. used DIW to build cathodes and anodes and assembled a full high-performance micro-battery.[34] We recently reported the fabrication of interdigitated graphene framework using DIW for remarkable micro-super-capacitors.[35] To date, the DIW-based fabrication of CSSEs or HSSEs was rarely reported owing to the difficulty in preparing 3D printable electrolyte inks. In this regard, the 3D printing of CSSEs and HSSEs with customized configuration is urgently demanded but challenging.

Herein, we report the DIW fabrication of LATP-based CSSEs and HSSEs with arbitrary shapes as well as high conductivities. To resolve the abovementioned ink issue, a formulated liquid is employed to obtain the pure LATP CSSE 3D printable ink. The obtained ink possesses suitable rheological behaviors and can be successfully extruded into free-standing CSSEs with different desired shapes and high conductivities up to 4.24×10^{-4} S cm^{-1}. Moreover, our DIW approach enables the direct printing of high-conductive LATP-based HSSEs. The corresponding solid-state LiFePO$_4$ (LFP)//Li battery exhibits a high discharge capacity of 150 mAh g^{-1} at 0.5 C and a good cycling stability during the cycling test at 60 °C. The achieved results demonstrate the enormous potential of 3D printed SSEs and offer a new fabrication platform for next-generation customized electrochemical energy storage devices.

The DIW procedure of LATP CSSE architectures is briefly illustrated in **Figure 1**. An extrusion-based 3D printer equipped with a syringe was employed to extrude the 3D printable ink driven by the pneumatic pressure. To realize the continuous and smooth extrusion, the ink formula as well as its dispersing state was essential for the printing process. To this end, the suitable dispersant was essential to disperse LATP powder to access the control of rheological properties for 3D printable ink. Rather than the direct use of single solvent as the dispersant, the formulated liquid with deionized (DI) water and isopropanol (IPA) in a certain volumetric ratio of 4:1 was applied to disperse the LATP powder. In the mixed liquid, IPA acted as the dispersant promotor for the better dispersing process while the DI water helped to keep the wet state of ink. By adding LATP powder in the formulated liquid, the obtained mixture was thoroughly grounded in an agate mortar until the ink was suitable for the DIW process as displayed in Figure 1a,b.

After the ink preparation, the ink was loaded into a syringe as shown in Figure 1c and the extrusion-based 3D printer was used to extrude LATP ink with different layers with programmed routines (Figure 1d,e). Finally, a post heat-treatment was proceeded to enhance the ceramic density and form the resultant LATP CSSE (Figure 1f). The DIW-based manufacturing process enabled the well control in the both electrolyte thicknesses and shapes, illustrating a huge advantage for the customized CSSE fabrication. For example, the thickness of LATP CSSE with 3 printing layers was appropriately 1.2 mm and this value would further increased by digitally printing growing layers.

A key way to evaluate the ink rheological behaviors is observing the ink flowing state during the extrusion process. For as-prepared LATP ink dispersed using the formulated liquid with DI water and IPA, the continuous ink extrusion was observed within 4 s as shown in **Figure 2**a and Movie S1 (Supporting Information). In comparison, with the same amount of DI water dispersant, a direct breaking point was easily found for the aqueous LATP ink as displayed in Figure 2b and Movie S2 (Supporting Information). The obvious difference in the ink flowing state revealed the different ink rheological behaviors of as-prepared inks and further influenced the layer-by-layer stacking process. The discontinuous ink flowing could not ensure the continuous materials stacking, resulting in the fail of 3D-structured construction. The rheological properties of extrudable ink were further measured (Figure 2c). It was observed that the viscosity values decreased when the shear stress values increased, revealing the shear-thinning non-Newtonian fluid behavior. It further confirmed the good printability of the ink obtained with the dispersant mixture of DI water and IPA and indicated a desired extrusion process as shown in the inset of Figure 2c.

**ADVANCED
SCIENCE NEWS**

www.advancedsciencenews.com

NANO · MICRO

small

www.small-journal.com
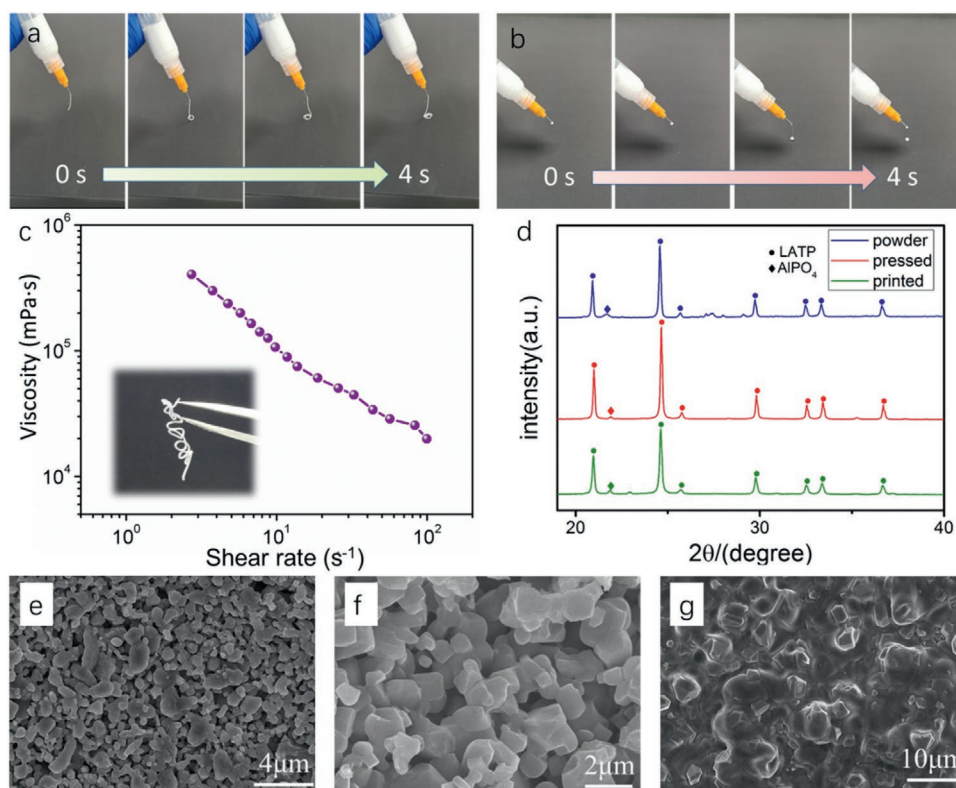
Figure 2. Photographs showing the extrusion process from a syringe for difference inks dispersed by a) the mixture of DI water and IPA, b) the pure DI water. c) Apparent viscosity values as a function of shear rate values for ink prepared with the dispersant mixture of DI water and IPA. The inset represents the corresponding extrusion state. d) XRD patterns of LATP powder, pressed pallet and 3D printed CSSE. SEM images of 3D printed LATP CSSE sintered at different temperatures of e) 850 °C, f) 950 °C, and g) 1050 °C.

To investigate the structural changes of as-prepared samples during the DIW process, X-ray diffraction (XRD) and scanning electron microscopic (SEM) measurements were conducted. As shown in Figure 2d, it was found that there was no significant difference in the phase composition for LATP powder, pressed pallet and 3D printed CSSE, which were all sintered at 950 °C. It indicated that the adding of formulated liquid did not influence the formation of main LATP phase during the DIW process of CSSEs.[36] The displayed peaks were mainly indexed to the LATP phase (JCPDS NO. 35-0754). A secondary phase of $AlPO_4$ was also found, which was consistent with previous literatures.[21,37,38] However, when sintered at different temperatures in a range of 850–1050 °C, as-printed CSSEs exhibited distinct differences in phases as shown in Figure S1 (Supporting Information). The peak intensities of $AlPO_4$ secondary phase became weaker with the growing sintering temperatures from 850 to 950 °C, while the intensities of $AlPO_4$ peaks directly exceeded those of LATP-pahse peaks when the sintering temperature came to 1050 °C. These results illustrated that the ideal sintering temperature was 950 °C for the 3D printed LATP CSSEs.

SEM measurements further revealed the structural evolution as detailed in Figure 2e–g. The obtained LATP powder showed a particle morphology with the average sizes of 1–2 μm (Figure S2, Supporting Information). The cross-sectional SEM images of 3D printed LATP CSSE revealed that the microcracks between the layers occurred as seen in Figure S3 (Supporting Information) suggesting an effect on the ionic conductivity.

When sintered at 1050 °C, the CSSE pallets showed a visible contraction, while this phenomenon was not obvious for the pallets sintered at 850 and 950 °C. Figure 2e–g further illustrated that the grain sizes increased with the growing sintering temperatures. The densification of 3D printed LATP CSSEs increased as well with growing sintering temperatures. The grain boundaries were obviously observed and the diameter of grains ranged from 1 to 2 μm for the 3D printed LATP CSSE sintered at 950 °C. With a further increased sintering temperature at 1050 °C, a glass state was presented (Figure 2g). This may be caused by the lithium volatilization, which led to the introduction of $LiTiOPO_4$ secondary phase (Figure S1, Supporting Information), which was an influencial factor for the delivered ionic conductivity.

The electrochemical behaviors of LATP CSSEs with different printing layers were measured using the electrochemical impedance spectroscopy (EIS) method. The obtained data was collected with a test frequency ranging from 0.1 Hz to 1 MHz. Impedance plots were used to analyze the bulk resistance (R_b) and interfacial resistance (R_i). The total resistance (R_t) was summed by $R_t = R_b + R_i$. Thus, the total conductivity (σ_t) could be calculated with the equation of $\sigma = d/A \times R_t$, where d and A represented CSSE thickness and area, respectively.[39] **Figure 3**a shows the measured impedance plots, where one or two semicircles at high frequencies and a spike in the low frequency region were both found for various 3D printed CSSEs. The semicircles may be attributed to the bulk, grain boundary

**ADVANCED
SCIENCE NEWS**
www.advancedsciencenews.com

NANO · MICRO
small
www.small-journal.com

and interfacial resistances, while the spike may due to the double-layer impedance at the contact between the blocking electrodes and CSSEs.[37] The calculated ionic conductivities of as-printed CSSEs decreased with growing printing layers (Figure 3b), which was consistent with previous reports.[40] The achieved ionic conductivity was up to 4.24×10^{-4} S cm^{-1} for LATP CSSE with 3 printing layers, while the ionic conductivities of LATP CSSE with 4, 5, and 6 printing layers were calculated to 2.34×10^{-4}, 2.14×10^{-4}, 1.38×10^{-4} S cm^{-1}, respectively. The electronic conductivity of CSSE with 3 printing layers was calculated to 1.55×10^{-8} S cm^{-1} and the relative density was calculated to 85.6%. Time-decaying current density of printed LATP CSSE was shown in Figure S4 (Supporting Information). It is worth noting that during the CSSE fabrication process the tableting and the mold were not utilized, indicating the saved energy and simplified procedure. The obtained results were still remarkable, demonstrating the great promise of DIW technique for the CSSEs fabrication.

To further investigate the effects of sintering temperatures during the post-treatment, the ionic conductivities of CSSEs with different sintering temperatures were further investigated (printing layer was fixed at 3). The ionic conductivities were 0, 0.48×10^{-4}, 1.55×10^{-4}, 4.24×10^{-4}, 2.05×10^{-4} S cm^{-1}, respectively, for 3D printed LATP CSSEs sintered ranging from 650 to 1050 °C. It is abovementioned that, with increasing sintering temperatures from 650 to 950 °C, the crystalline increased which may attribute to the increased ionic conductivity of obtained CSSE. However, with the further increased sintering temperature at 1050 °C, the conductivity showed a subsequent decrease, which may be caused by the presence of

the LiTiOPO$_4$ secondary phase.[41,42] In this regard, 950 °C was the most suitable sintering temperature for 3D printed LATP CSSEs during the post-treatment.

The galvanostatic cycling result of Li/3D printed LATP CSSE/Li symmetric cell was shown in Figure 3d. The Li plating/stripping was implemented at 60 °C at the current density of 0.05 mA cm^{-2} and each cycle was 0.5 h. After cycling for over 100 h, the polarization voltage was found to be less than 0.5 V. It clearly demonstrated the great advantage of our 3D printed CSSE for desirable solid-state energy storage applications.

For practical applications, a customized battery geometry is usually demanded under different conditions. To this end, the SSEs manufacturing technology with the capability to ensure the geometry customization is highly significant. To demonstrate the customization advantage of this work in geometry, CSSEs with different geometries were constructed just by adjusting the printing routines. As displayed in **Figure 4**a–c, three types of customized CSSE with "L" shape, "T" shape, and "+" shape were printed using the same DIW method. Meanwhile, the thickness of obtained CSSEs can still be well controlled in a digital way. In this work, 3D printed CSSEs with different shapes were designed to possess the same cross-sectional area. The impedance plots of these CSSEs with "L" shape, "T" shape, and "+" shape were shown in Figure 4d–f and their ionic conductivities were 4.05×10^{-4}, 4.17×10^{-4}, and 3.95×10^{-4} S cm^{-1}, respectively, which were very close to that of the rectangular CSSE sintered at 950 °C.

To further demonstrate the great potential of the employed DIW approach, the printing of LATP-based HSSE was also conducted. The printing process was schematically displayed
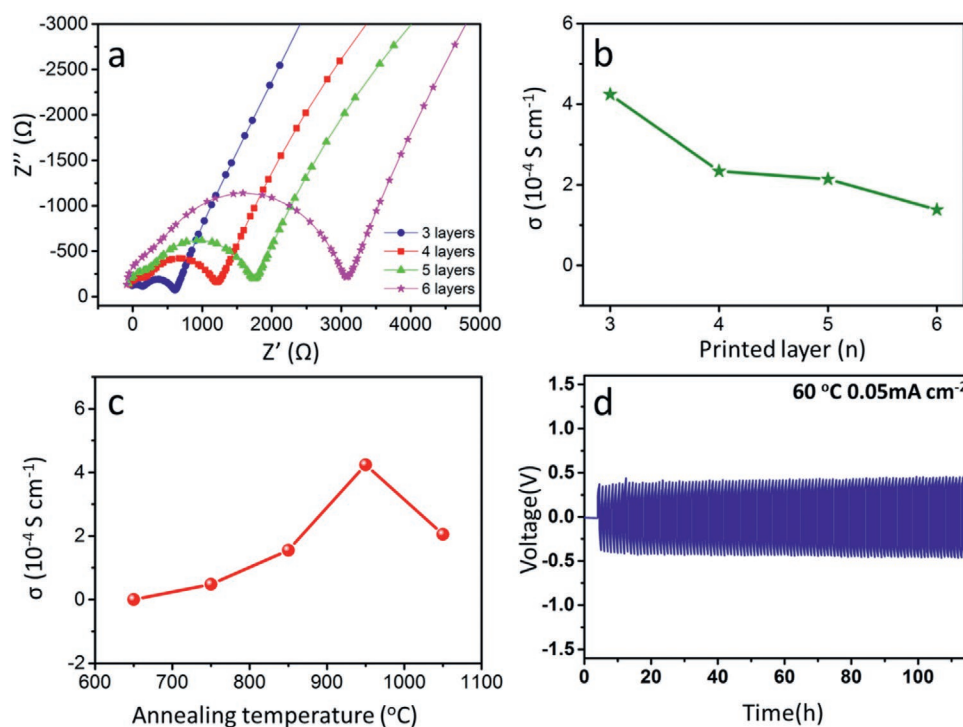
Figure 3. a) Impedance plots of as-printed LATP CSSE sintered at 950 °C for 6 h with different printing layers. b) Ionic conductivities of as-printed LATP CSSE sintered at 950 °C for 6 h with different printing layers. c) Ionic conductivities of as-printed LATP CSSE with 3 printing layers with different sintering temperatures. d) Galvanostatic cycles of Li/LATP CSSE/Li symmetric cell.
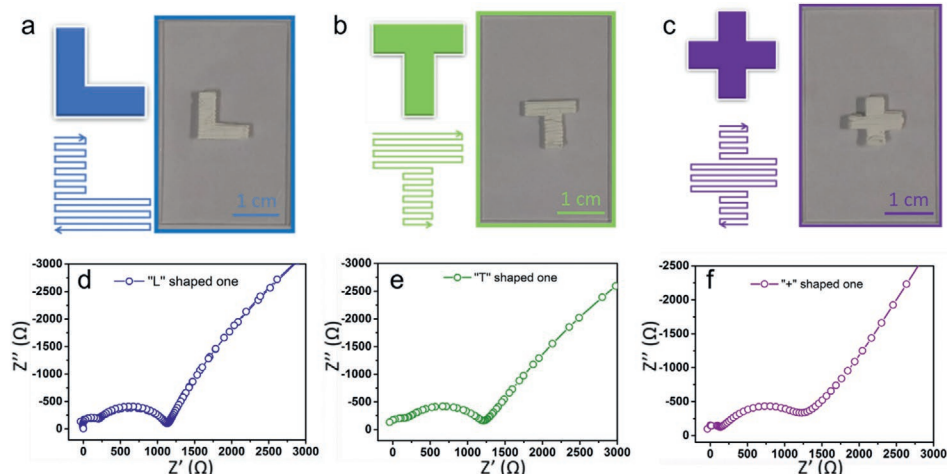
Figure 4. Schematics, printing routines, and optical images of as-printed LATP CSSEs with various geometries of a) "L" shape, b) "T" shape, and c) "+" shape. d–f) Corresponding impedance plots of as-printed LATP CSSEs with various geometries.

in **Figure 5**a, where poly(ethylene oxide) (PEO) and lithium bis(trifluoromethane)sulfonimide (LiTFSI) were introduced for the resultant HSSE ink formation. 3D printed LATP-based HSSEs with different geometries were also successfully realized as displayed in Figure 5b, indicating the high versatility of our approach. SEM images shown in Figure 5c demonstrated that the components were uniformly dispersed in the obtained ink. As shown in the thermogravimetric (TG) curve (Figure 5d), the decomposition temperature of the HSSE was above 300 °C, reflecting that the HSSE could be utilized at the elevated temperature. The printing of LATP-based HSSE was conducted on LFP cathode (inset in Figure 5e) and the LFP/3D printed LATP-based HSSE/Li battery can thus be fabricated without the adding

of any liquid electrolyte. The first charge and discharge profiles of assembled solid-state battery were shown in Figure S5 (Supporting Information), revealing the obvious charge–discharge plateau and high discharge capacity of 150 mAh g^{-1} at 0.5 C. The superior cycling performance was also found with a high capacity retention of 84% after 100 cycles (Figure 5e). The rate performance of solid-state battery was further measured at 60 °C at different rates from 0.1 to 0.5 C (Figure 5f). The result demonstrated that the battery capacity could be largely recovered when the rate returned back to 0.1 C. This was a clear indication of good rate capability for the obtained all-solid-state battery.

In summary, using a simple DIW method, we reported various well-dispersed LATP-based 3D printable inks which
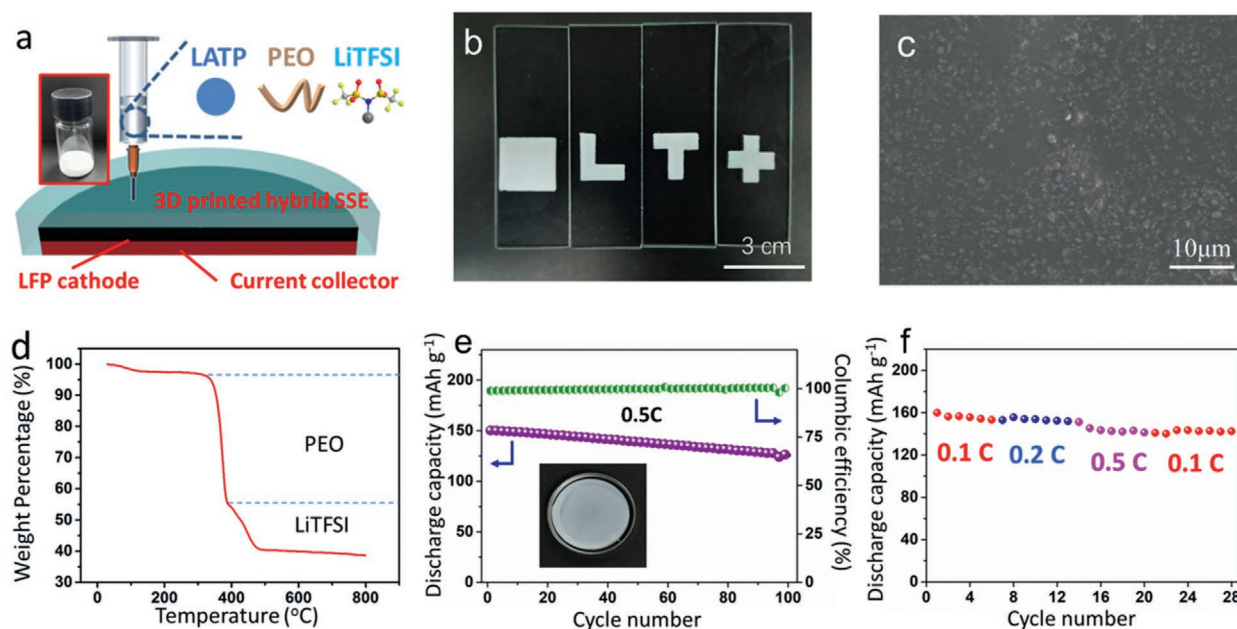
Figure 5. a) Schematic of DIW of LATP-based HSSE. The inset is the photograph of obtained ink. b) Photograph of LATP-based HSSEs with various geometries. c) SEM image and d) TG curve of LATP-based HSSE. e) Cycling performance at 0.5 C and f) rate performance of LFP/LATP-based HSSE/Li battery.

showed excellent rheological properties. Based on the obtained inks, free-standing LATP-based CSSE and HSSE were both fabricated where the geometries and thicknesses could be precisely controlled in the digital manner. With the optimized printing layer, the resultant LATP CSSE delivered remarkable ionic conductivity up to 4.24×10^{-4} S cm^{-1}. By re-designing printing routines, customized configurations including "L", "T," and "+" shapes were realized for LATP CSSE and HSSE. Moreover, using this printing method, the LATP-based HSSE can be directly constructed on LFP cathode for a solid-state lithium battery, where a remarkably high discharge capacity of 150 mAh g^{-1} was obtained at 0.5 C at 60 °C. This study provides an advanced manufacturing platform for the customized SSEs fabrication, showing the enormous potential for next-generation state-of-the-art electrochemical energy storage systems.

Experimental Section

LATP Powder Preparation: LATP powder was prepared by the conventional solid state method,[43,44] where lithium carbonate (AR, ≥ 99.9%), aluminum oxide (AR, ≥ 99.9%), titanium dioxide (AR, ≥ 99.9%), and ammonium dihydrogen phosphate (AR, ≥ 99.9%) were mixed through wet ball-milling with stoichiometric amounts. Then, a sintering process with a 700 °C heating for 4 h was conducted to get the LATP powder. The obtained powder was ball-milled for 10 h before the DIW printing.

DIW of LATP CSSE: To obtain well-dispersed printable inks, LATP powder was mixed with the formulated liquid (mixture of DI water and IPA with a volume ratio of 1:4) by agate mortar and the concentration of LATP in obtained ink was 1 g ml^{-1}. Then, the ink was loaded in the syringe with a nozzle (≈330 μm inner diameter). A pneumatic-driven extrusion-based 3D printer was employed to conduct the DIW process on the quartz glass. Various customized shapes were designed with different printing layers (3–6). The freeze-drying was subsquently carried out for 12 h where the cold trap temperature was −50 °C. The high-temperature sintering was then employed for 6 h with different sintering temperatures ranging from 650 to 1050 °C to obtain the final 3D printed LATP CSSEs.

DIW of LATP-Based HSSE: For the 3D printable LATP-based HSSE ink, LiTFSI and PEO were dissolved in acetonitrile at 70 °C. Then, the LATP powder was added into the above mixture to obtain the 3D printable ink. The mole ratio of –CH$_2$-CH$_2$O– (EO)/Li was controlled to be 18:1 and the amount of LATP was 40 wt%. Then, the LATP-based HSSE was obtained using the DIW method. For the solid-state battery assembly, LATP-based HSSE was directly printed on cathode which was composed of LFP, poly(vinylidene fluoride) (PVDF) and Super P with a mass ratio of 6:2:2. Then, the volatilization of solvent was awaited in glovebox for two days in prior to the assembly of LFP/3D printed LATP-based HSSE/Li battery.

Structural Characterization and Electrochemical Measurements: Scanning electron microscopic (SEM) images were collected using a Hitachi-SU8010 field-emission scanning electron microscope. XRD patterns were recorded with D8 Advance X-ray diffractometer using Cu Kα1 radiation (λ = 0.15405 nm). The patterns were scanned in steps of 0.02° with counting for 0.1 s at each step ranging from 10° to 80° (2θ angle). The ink rheological property was measured by Anton Paar MCR302 rheometer.

EIS was measured by Zennium X electrochemical workstation in the frequency range from 0.1 Hz to 10 MHz. Both sides of samples were polished and sputtered with Au before measurements. THALES software was used for the data acquisition and processing and the measurement was conducted at 25 °C. The battery was measured by LANHE CT2001A at 60 °C. TG analysis was evaluated by STA 409 PC (Germany NETZSCH) from 30 to 800 °C with a heating rate of 10 °C min^{-1} under nitrogen atmosphere.

Supporting Information

Supporting Information is available from the Wiley Online Library or from the author.

Conflict of Interest

The authors declare no conflict of interest.

[1] B. K. Zhang, R. Tan, L. Y. Yang, J. X. Zheng, K. C. Zhang, S. J. Mo, Z. Lin, F. Pan, *Energy Storage Mater.* **2018**, *10*, 139.

[2] A. Varzi, R. Raccichini, S. Passerini, B. Scrosati, *J. Mater. Chem. A* **2016**, *4*, 17251.

[3] Y. Kato, S. Hori, T. Saito, K. Suzuki, M. Hirayama, A. Mitsui, M. Yonemura, H. Iba, R. Kanno, *Nat. Energy* **2016**, *1*, 16030.

[4] S. Chu, A. Majumdar, *Nature* **2012**, *488*, 294.

[5] J. M. Tarascon, M. Armand, *Nature* **2001**, *414*, 359.

[6] J. Cabana, L. Monconduit, D. Larcher, M. R. Palacin, *Adv. Mater.* **2010**, *22*, E170.

[7] E. Quartarone, P. Mustarelli, *Chem. Soc. Rev.* **2011**, *40*, 2525.

[8] Y. S. Hu, *Nat. Energy* **2016**, *1*, 16042.

[9] J. W. Fergus, *J. Power Sources* **2010**, *195*, 4554.

[10] W. Xia, B. Xu, H. Duan, Y. Guo, H. Kang, H. Li, H. Liu, *ACS Appl. Mater. Interfaces* **2016**, *8*, 5335.

[11] T. Matsuyama, A. Sakuda, A. Hayashi, Y. Togawa, S. Mori, M. Tatsumisago, *J. Solid State Electrochem.* **2013**, *17*, 2697.

[12] K. Xu, *Chem. Rev.* **2004**, *104*, 4303.

[13] J. B. Goodenough, K. S. Park, *J. Am. Chem. Soc.* **2013**, *135*, 1167.

[14] A. Hayashi, K. Noi, A. Sakuda, M. Tatsumisago, *Nat. Commun.* **2012**, *3*, 856.

[15] F. Wu, N. Chen, R. J. Chen, Q. Z. Zhu, J. Qian, L. Li, *Chem. Mater.* **2016**, *28*, 848.

[16] W. D. Richards, Y. Wang, L. J. Miara, J. C. Kim, G. Ceder, *Energy Environ. Sci.* **2016**, *9*, 3272.

[17] J. B. Goodenough, H. Y.-P. Hong, J. A. Kafalas, *Mater. Res. Bull.* **1976**, *11*, 203.

[18] M. A. Subramanian, R. Subramanian, A. Clearfield, *Solid State Ionics* **1986**, *18*, 562.

[19] H. Aono, E. Sugimoto, Y. Sadaaka, N. Imanaka, G. Adachi, *J. Electrochem. Soc.* **1989**, *136*, 590.

[20] H. Aono, E. Suginoto, *J. Am. Ceram. Soc.* **1996**, *79*, 2786.

[21] S. S. Duan, H. Y. Jin, J. X. Yu, E. N. Esfahani, B. Yang, J. L. Liu, Y. Z. Ren, Y. Chen, L. H. Lu, X. C. Tian, S. E. Hou, J. Y. Li, *Nano Energy* **2018**, *51*, 19.

[22] J. W. Stansbury, M. J. Idacavage, *Dent. Mater.* **2016**, *32*, 54.

[23] P. Wu, J. Wang, X. Y. Wang, *Automat. Constr.* **2016**, *68*, 21.

[24] T. T. Wohlers, T. Caffrey, *Wohlers Report 2014: 3D Printing and Additive Manufacturing State of the Industry Annual Worldwide Progress Report*, Wohlers Associates, Fort Collins, CO **2014**.

[25] H. D. Carlton, A. Haboub, G. F. Gallegos, D. Y. Parkinson, A. A. MacDowell, *Mater. Sci. Eng., A* **2016**, *651*, 406.

[26] G. Postiglione, G. Natale, G. Griffini, M. Levi, S. Turri, *Composites, Part A* **2015**, *76*, 110.

[27] Y. Song, Y. Li, W. Song, K. Yee, K. Y. Lee, V. L. Tagarielli, *Mater. Des.* **2017**, *123*, 154.

[28] X. C. Tian, K. Tang, H. Y. Jin, T. Wang, X. W. Liu, W. Yang, Z. C. Zou, S. E. Hou, K. Zhou, *Carbon* **2019**, *155*, 562.

[29] L. Zhou, W. Ning, C. Wu, D. Zhang, W. Wei, J. Ma, C. Li, L. Chen, *Adv. Mater. Technol.* **2019**, *4*, 1800402.

[30] S. Shan, S. H. Kang, J. R. Raney, P. Wang, L. C. Fang, F. Candido, J. A. Lewis, K. Bertoldi, *Adv. Mater.* **2015**, *27*, 4296.

[31] E. B. Duoss, T. H. Weisgraber, K. Hearon, C. Zhu, W. Small Iv, T. R. Metz, J. J. Vericella, H. D. Barth, J. D. Kuntz, R. S. Maxwell, C. M. Spadaccini, T. S. Wilson, *Adv. Funct. Mater.* **2014**, *24*, 4905.

[32] F. P. W. Melchels, J. Feijen, D. W. Grijpma, *Biomaterials* **2010**, *31*, 6909.

[33] J. Z. Manapat, Q. Chen, P. Ye, R. C. Advincula, *Macromol. Mater. Eng.* **2017**, *302*, 1600553.

[34] K. Sun, T. S. Wei, B. Y. Ahn, J. Y. Seo, S. J. Dillon, J. A. Lewis, *Adv. Mater.* **2013**, *25*, 4539.

[35] T. Wang, L. Li, X. C. Tian, H. Y. Jin, K. Tang, S. E. Hou, H. Zhou, X. H. Yu, *Electrochim. Acta* **2019**, *319*, 245.

[36] S. Soman, Y. Iwai, J. Kawamura, A. Kulkarni, *J. Solid State Electrochem.* **2012**, *16*, 1761.

[37] S. S. Duan, J. X. Yu, Y. W. Sun, A. L. Li, S. L. Chen, K. Qu, Z. P. Ding, Z. X. Liu, Y. H. Li, C. Huang, M. Liu, J. L. Liu, J. P. Shi, B. Y. Huang, X. C. Tian, S. E. Hou, S. H. Xie, Y. Y. Liu, P. Gao, J. Y. Li, H. Y. Jin, *J. Power Sources* **2020**, *449*, 227574.

[38] W. Xiao, J. Y. Wang, L. L. Fan, J. J. Zhang, X. F. Li, *Energy Storage Mater.* **2019**, *19*, 379.

[39] X. X. Xu, Z. Y. Wen, X. L. Yang, L. D. Chen, *Mater. Res. Bull.* **2008**, *43*, 2334.

[40] K. Fu, Y. B. Wang, C. Y. Yan, Y. G. Yao, Y. N. Chen, J. Q. Dai, S. Lacey, Y. B. Wang, J. Y. Wan, T. Li, Z. Y. Wang, Y. Xu, L. B. Hu, *Adv. Mater.* **2016**, *28*, 2587.

[41] B. Key, D. J. Schroeder, B. J. Ingram, J. T. Vaughey, *Chem. Mater.* **2012**, *24*, 287.

[42] R. Kali, A. Mukhopadhyay, *J. Power Sources* **2014**, *247*, 920.

[43] K. Arbi, W. Bucheli, R. Jiménez, J. Sanz, *J. Eur. Ceram. Soc.* **2015**, *35*, 1477.

[44] H. Morimoto, M. Hirukawa, A. Matsumoto, T. Kurahayashi, N. Ito, S. Tobishima, *Electrochemistry* **2014**, *82*, 870.